Dual-bell nozzle with fluidic control of transition for space launchers

Graphical Abstract

Dual-bell nozzle with fluidic control of transition for space launchers

Andrea Ferrero, Antonietta Conte, Emanuele Martelli, Francesco Nasuti, Dario Pastrone

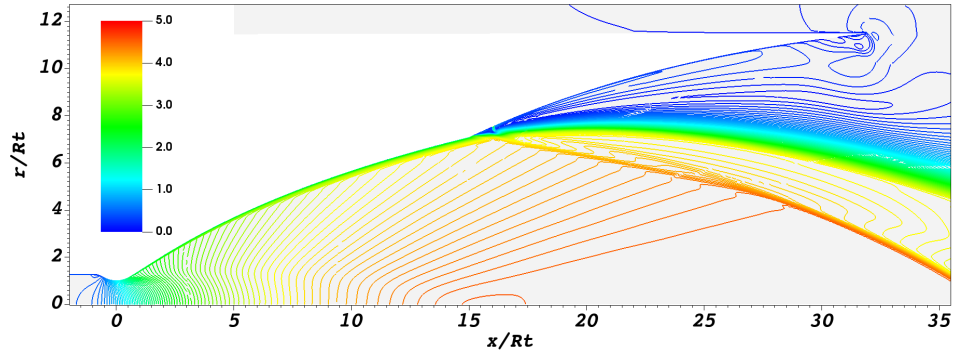

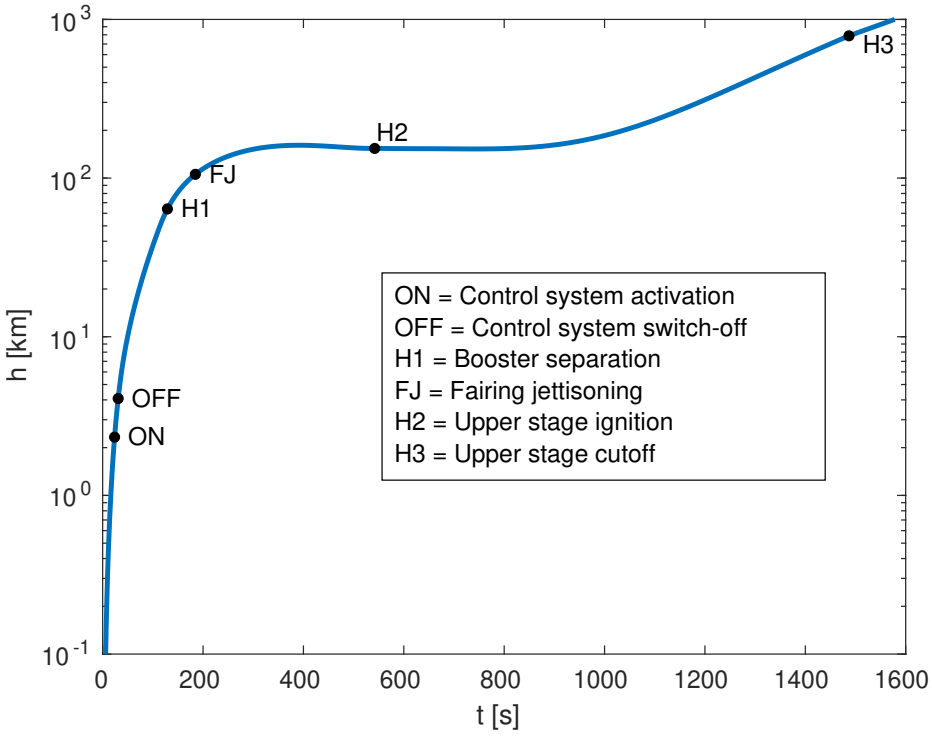

Highlights

Dual-bell nozzle with fluidic control of transition for space launchers

Andrea Ferrero, Antonietta Conte, Emanuele Martelli, Francesco Nasuti, Dario Pastrone

- A dual-bell nozzle in the core engine of the Ariane 5 configuration would lead to significant payload increase
- Side loads during mode transition represent a critical obstacle to the implementation of this solution
- Fluidic control is studied as a method to reduce side loads and make the solution feasible

Dual-bell nozzle with fluidic control of transition for space launchers

Andrea Ferrero[a,*], Antonietta Conte[a], Emanuele Martelli[b], Francesco Nasuti[c], Dario Pastrone[a]

[a] *Department of Mechanical and Aerospace Engineering, Politecnico di Torino, Corso Duca degli Abruzzi 24, Turin, 10129, Italy*
[b] *Department of Engineering, Università degli Studi della Campania Luigi Vanvitelli, Via Roma 29, Aversa, 81031, Italy*
[c] *Department of Mechanical and Aerospace Engineering, Sapienza Università di Roma, Via Eudossiana 18, Rome, 00184, Italy*

Abstract

The dual-bell nozzle is a promising concept for improving the performance of space launchers. It is characterised by the presence of two altitude-dependent working modes which allow to reduce non-adaptation losses. However, the transition between the two working modes usually takes place prematurely and dangerous side loads might be observed. In this work, fluidic control is investigated as a potential method to delay the transition and limit the risk of side loads. A launcher configuration similar to the Ariane 5 with a dual-bell nozzle in the core engine is considered. First, a parametric optimisation is performed to identify the dual-bell geometry that maximises the payload mass delivered into geostationary transfer: a preliminary model is adopted to describe the dual-bell mode transition and a fast and reliable in-house trajectory optimisation code is used to optimise the ascent trajectory. The flow field in the optimal geometry is then investigated by CFD simulations to verify the effectiveness of fluidic control. Finally, the CFD study results are used to model the dual-bell mode transition and trajectory optimisation is performed again. The proposed solution is characterised by a large payload gain (approximately 1.5 metric tons) with respect to the reference launcher. The simulations showed that fluidic control reduces the order of magnitude of

*Corresponding author
Email address: andrea_ferrero@polito.it (Andrea Ferrero)

side loads which can arise during transition, showing its potential as enabling technology for the application of dual-bell nozzles on real launchers.

Keywords: Dual-bell nozzle, Side loads, Fluidic control, Trajectory optimisation

1. Introduction

Rocket engines used in the first stage of space launchers work from sea-level to almost vacuum conditions. An example is represented by the Vulcain 2 liquid rocket engine used in the Ariane 5 launcher. The area ratio of its nozzle is limited by the necessity to avoid uncontrolled separation and dangerous side loads at lift-off. This limitation has a significant impact on the engine's performance when high altitudes are reached.

In order to avoid such limitations of classical bell nozzles, several alternatives have been proposed and studied [1]: nozzles with fixed insert [2], nozzles with temporary insert [3], Expansion-Deflection nozzles [1], nozzles with forced gas injection [4], plug nozzles [5], dual-bell nozzles [6–11], vented nozzles [12], nozzles with separation avoiding devices [13, 14], nozzles controlled by plasma actuators [15] and nozzle with gas injection [16]. Among them, the dual-bell nozzle represents a promising solution because of its effectiveness and the minor changes it requires with respect to conventional nozzles. The basic idea is to consider a bell shaped nozzle connected to a bell shaped extension by means of an inflection: the discontinuity in the contour slope allows anchoring the separation line and avoiding side loads at low altitudes. When the external pressure reduces below a threshold value, transition occurs and full flow working conditions are obtained. The presence of these two working modes significantly improves the specific impulse, which strongly affects launcher performance especially at higher altitudes where actual payload mass fraction is larger. However, two drawbacks related to the transition process have been individuated during the various feasibility studies. The first one is associated to an early transition to the high-altitude working mode which would limit the performance gain [8]. The second one is far more critical as it is a possible obstacle to the real implementation of this solution: significant side loads can be observed during the transition process [17, 18]. Furthermore, Verma et al.[19] performed an experimental study on the effect of ambient pressure fluctuations on the uncontrolled transition: their results showed that external pressure fluctuations can induce a

flip-flop phenomenon which can represent a significant problem in real-flight operation, especially when the launcher experiences the buffeting phase of flight. Finally, the design is complicated by the uncertainty on transition prediction: numerical simulations are affected by epistemic uncertainty on turbulence modelling and experimental tests are limited by scalability effects related to the Reynolds number [20].

Several strategies have been investigated to control the transition, such as fluidic control [21–25], film cooling [26–29], and mixture ratio variation [29]. Fluidic control is a promising strategy which consists in injecting fluid through a slot near the inflection point; the injected fluid represents an obstacle to the supersonic flow and allows control of the separation line. The previous numerical and experimental studies available in the literature showed the effectiveness of fluidic control of transition in small scale dual-bell nozzles characterised by small values of the expansion ratio. In the present work, the effects of fluidic control on a full scale engine are evaluated and the following points are investigated: the feasibility of the control in terms of control mass flow rate, the effects, on the launcher trajectory and performance, of the resulting engine performance and added fluid/inert masses, the side-loads reduction during dual-bell mode transition.

In particular, a configuration inspired by the Ariane 5 launcher with a dual-bell in the core engine is studied, and fluidic control is investigated as a potential strategy to delay the transition and limit the magnitude of side loads. First of all, a preliminary optimisation study is performed on the dual-bell geometry and on the launcher trajectory to maximise the payload gain. This preliminary optimisation is based on the assumption that fluidic control is able to increase the transitional nozzle pressure ratio (NPR) to the optimal value corresponding to the best performance. As a second step, the flow field inside the optimal dual-bell nozzle is investigated by CFD simulations for several values of NPR to verify the fluidic control effectiveness. The CFD study enabled the determination in more detail of the fluidic control requirements in terms of mass flow rate and activation time. These data are then used to update the optimal solution and to verify the potential of fluidic control as an enabling technology for the application of dual-bell nozzles on real launchers.

2. Preliminary optimisation for dual-bell geometry selection

A coupled trajectory/nozzle optimization is carried out to identify a suitable dual-bell geometry. A launcher similar to the Ariane 5 is considered in which the Vulcain 2 nozzle is substituted by a dual-bell nozzle with a constant pressure extension. This study is made in analogy with [30] where the impact of the dual-bell nozzle on the payload mass delivered into a reference geosynchronous transfer orbit (GTO) by Ariane 5 ECA was evaluated. Stark et al. [30] investigated several dual-bell nozzle contours with constant pressure extension by changing the area ratio of the first bell (ϵ_1) and the inflection angle (α). The best solution was identified using both an analytical approach based on the ideal rocket velocity increment and a trajectory optimisation procedure. They showed that a significant payload gain can be obtained. In the present work the goal is still to find the dual-bell geometry that maximise the payload mass inserted into a reference GTO launching from CGS (Kourou), but a controlled dual-bell mode transition is assumed. The considered dual-bell nozzle is characterised by a first bell obtained by the method of characteristic (truncated ideal contour nozzle) followed by a constant pressure extension. Two free parameters are considered to define the dual-bell nozzle geometry: the inflection angle (α) and the truncation percentage (λ) of the second bell. The reference contour for the second bell is a constant pressure contour ending when it reaches the direction of nozzle axis. The actual bell is obtained by truncating the second bell contour to a certain fraction (λ) with respect to the reference one. The design parameters are highlighted in Figure 1 where the axial x and radial r coordinates are normalised with respect to the throat radius R_t. It is worth noting that the area ratio of the first bell is kept fixed ($\epsilon_1 = 50$) according to the best configuration reported in [30], whereas the introduction of the truncation percentage (λ) of the second bell allows for beneficial nozzle weight reduction.

The design parameters are investigated in the intervals $7° < \alpha < 17°$ and $0.5 < \lambda < 1$, but two size constraints are imposed on the engine length (L<4.5 m) and maximum expansion ratio ($\epsilon_2 < 150$). These values are in line with the limitations chosen by [30] which are determined by the launch pad margins. For each nozzle geometry, the ascent trajectory is optimised using a fast and efficient in-house solver based on the optimal control theory [31], similarly to previous related works [14, 15].

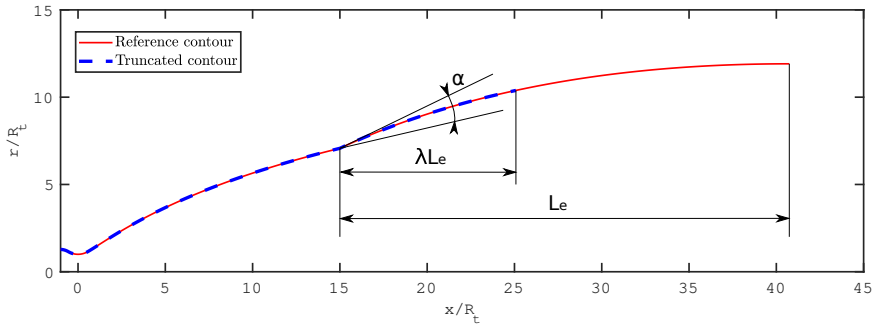

Figure 1: Dual bell nozzle with design parameters α and λ.

Table 1: Reference launch vehicle [14].

Stage	m_p tons	F_{vac} kN	m_s tons	$I_{sp,vacm}$ s	t_b s	A_e m^2	
Booster (each of 2)	480.40	-	80.60	274.0	129$^{(*)}$	15.38	
Core Engine	-	1359	16.00	429.0	532$^{(*)}$	3.42	
Upper stage	-	14.54	3.42	445.5	945	0.81	
Fairing	-	-	3.03	-	-	-	-

(*) = time from lift off

2.1. Trajectory optimisation

The trajectory optimization approach is briefly described in the following. Further details can be found in [14]. A point mass rocket is considered and the state equations provide the derivative of position $\mathbf{r}$, velocity $\mathbf{v}$ and rocket mass m. The vectorial form of equations of motion, written in non-dimensional form to improve the integration's numerical accuracy, are

$$\frac{\mathrm{d}\mathbf{r}}{\mathrm{d}t} = \mathbf{v} \qquad \frac{\mathrm{d}\mathbf{v}}{\mathrm{d}t} = \mathbf{g} + \frac{\mathbf{F}-\mathbf{D}}{m} \qquad \frac{\mathrm{d}m}{\mathrm{d}t} = -\frac{|\mathbf{F}|}{c^* C_F} \tag{1}$$

where $\mathbf{F}$, $\mathbf{D}$, $\mathbf{g}$, c^* and C_F represent thrust, aerodynamic drag, gravity acceleration, characteristic velocity and thrust coefficient, respectively.

A launcher with characteristics similar to those of the European Ariane 5 ECA[33] is considered. Table 1 presents the main characteristics of the primary propulsion systems: propellent mass m_p, vacuum thrust F_{vac}, structural mass m_s, vacuum specific impulse $I_{sp,vacm}$, burning time t_b and nozzle

Table 2: Reference mission.

Apogee (km)	Perigee (km)	Inclination (deg)	Periaxis arg. (deg)	Ref.
35943	250	6.0	178.0	[32]

Table 3: Ascent phases.

N.	Phase	Type
1	vertical ascent to clear launch pad	fixed length 73 m, about 5 s
2	rotation phase	optimal thrust direction and duration
3	ascent with booster	zero-lift gravity-turn, ends at SRM burnout
4	main engine only with fairing	zero-lift gravity-turn, fixed time 45 s
5	main engine only with fairing	optimal thrust direction, ends when heat flux is 1135 W/m^2
6	main engine only w/o fairing	optimal thrust direction, ends at propellant depletion
7	coast arc	fixed time for staging, 10 s
8	upper-stage burn	optimal thrust direction, ends at propellant depletion
9	coast arc	ends at GTO apogee

exit area A_e. The payload inserted into a reference GTO orbit (apogee altitude 35943 km, perigee altitude 250 km, inclination 6.0 deg, periaxis argument 178.0 deg) is maximized for each given dual-bell geometry. Since all the other masses are kept constant, the lift-off mass is dependent on the payload. The trajectory is split into the phases outlined in Table 3.

The theory of optimal control[34, 35] is applied to optimize the trajectory. An adjoint variable is associated to each equation and the Hamiltonian is defined

$$H = \boldsymbol{\lambda_r}\mathbf{v} + \boldsymbol{\lambda_v}\left(\frac{\mathbf{r}}{|\mathbf{r}|^3} + \frac{\mathbf{F}-\mathbf{D}}{m}\right) - \lambda_m \frac{F}{c} \tag{2}$$

The optimal control theory provides the Euler-Lagrange equations for the adjoint variables $\lambda_\mathbf{r}$, $\lambda_\mathbf{v}$ and λ_m

$$\frac{\mathrm{d}\boldsymbol{\lambda_r}}{\mathrm{d}t} = -\frac{\mathrm{d}H}{\mathrm{d}\mathbf{r}} \qquad \frac{\mathrm{d}\boldsymbol{\lambda_v}}{\mathrm{d}t} = -\frac{\mathrm{d}H}{\mathrm{d}\mathbf{v}} \qquad \frac{\mathrm{d}\lambda_m}{\mathrm{d}t} = -\frac{\mathrm{d}H}{\mathrm{d}m} \tag{3}$$

In agreement with Pontriagyn's maximum principle, the optimal controls maximize H . When its direction is free (phases 2, 5, 6 and 8) the thrust must be parallel to the velocity adjoint vector λ_V. On the other hand, thrust direction is vertical during phase 1 and parallel to the relative velocity in phases 3 and 4.

The theory of optimal control also provides boundary conditions for optimality at the boundaries of each phase, here omitted for the sake of conciseness [35]. The resulting multipoint boundary value problem, is solved by a procedure[31] based on Newton's method. Tentative values are initially chosen for the problem unknowns and progressively modified to satisfy the boundary conditions.

The lift-off, here assumed as time reference, occurs about 7 seconds after core engine ignition. Separation of boosters occurs at the reference time H1 (129 s). The fairing is jettisoned during the core engine flight phase as soon as aero-thermodynamic flux levels are below 1135 W/m^2 (reference time FJ). After main-stage cutoff and separation, the upper stage ignition occurs (reference time H2). The indirect trajectory optimization maximizes the payload, i.e., the mass at upper stage cutoff (reference time H3) .

2.2. Dual-bell assumptions and results

The nozzle mass is estimated by assuming a uniform weight distribution ($35\ kg/m^2$) evaluated from the data reported by [30]. The thrust contribution of the base is evaluated by performing an inviscid CFD simulation. The aspiration drag in the low altitude working condition is assumed as negligible, while the thrust contribution provided by the extension in the high-altitude working mode is easily computed by considering a Prandtl-Meyer expansion centred at the inflection point.

The simulations are performed assuming that the secondary injection is activated (NPR_{ON}) when the natural transitional NPR is reached. The natural transitional NPR is estimated by means of the Schmucker criterion [36] in this preliminary evaluation. The secondary injection is deactivated (NPR_{OFF}) when the launcher reaches the optimal transitional NPR which guarantees the best performance of the dual-bell nozzle. The optimal NPR is determined by the condition in which the dual-bell provides the same thrust in both working modes.

The mass flow rate $\dot{m}_i$ used for the fluidic control is preliminary assumed to be 3 % of the main combustion chamber mass flow $\dot{m}$. A mass budget of m_{CS} =500 kg is allocated for the fluidic control system, including both dry masses and the control fluid mass which is reduced in time according to the prescribed injection mass flow rate. The results of this preliminary parametric study are reported in Figure 2 which shows the payload gain as a function of the design parameters α and λ. The plot also shows the constraint limits:

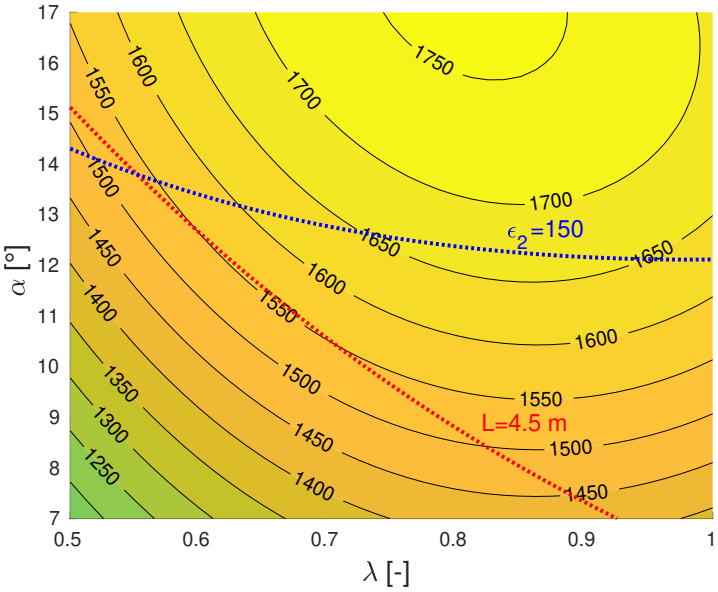

Figure 2: Optimisation results: payload gain (kg) as a function of design parameters. Red and blue dotted curves represents nozzle length constraint (L<4.5 m) and maximum expansion ratio constraint ($\epsilon_2 < 150$), respectively.

feasible solutions are localised below both curves. To accurately determine the constrained optimal point, an optimisation procedure is implemented in Matlab by using the active-set algorithm for constrained optimisation [37]. The algorithm performs a line search at each iteration: the relative bound on line search step length is set to 10^{-6}. It is particularly important to limit the step during the optimization process in order to consider small perturbations between a candidate solution and the next one: this greatly improves the convergence of the trajectory optimization algorithm which uses the trajectory computed at the previous step as initial guess for the next step. The optimal solution is characterised by the parameters reported in Table 4. The optimisation shows that a significant payload gain ($\Delta m_{PL} = 1556$ kg) is obtained with respect to the baseline configuration. It is worth noting that the control system is activated for a short time during which the launcher climbs from $h_{ON} = 5$ km to $h_{OFF} = 13$ km: the required control fluid mass is 230 kg.

Table 4: Preliminary optimal solution assuming $\dot{m}_i/\dot{m} = 0.03$ and $m_{CS} = 500$ kg

$\alpha[^\circ]$	11.46
λ [-]	0.6552
h_{ON} [km]	5
h_{OFF} [km]	13
NPR_{ON} [-]	222
NPR_{OFF} [-]	775
Δm_{PL} [kg]	1556

3. Fluidic control of transition

The flow field inside the optimal dual-bell nozzle is numerically studied to determine the required properties of the secondary injection at optimal NPR. Specifically, the mass flow needed to control the transition, the value of the natural transitional NPR (which determines NPR_{ON}) and the maximum NPR that can be obtained using the fluidic control (i.e maximum allowable NPR_{OFF}), are searched for. A preliminary parametric study showed that it is not possible to increase the transitional NPR up to the optimal value (NPR=775) [38]. However, the impact of the transitional NPR on the final payload is relatively small because the transition takes place when the boosters are still active. This fact suggests the choice of an alternative solution in which the secondary injection is used to significantly increase the transitional NPR even if the optimal transitional NPR is not reached: the goal is to minimise the occurrence of side loads by keeping the separation line fixed at the inflection point (where the magnitude of the wall pressure gradient is very large) and then letting transition take place by deactivating the secondary injection.

The simulations are carried out by numerically solving the Reynolds-averaged Navier-Stokes (RANS) equations based on an adaptive version of the Spalart and Allmaras model [39], which applies a compressibility correction [40] only in the shear layer and has no effect on the production term in the boundary layer [24]. The flow is assumed to be 2-D axisymmetric, steady, and compressible. An ideal gas with a constant specific heat ratio $\gamma = 1.14$ is considered. Viscosity is evaluated by using the Sutherland's law for water which is the main combustion product. The nozzle wall is considered adiabatic. A parallel implicit code based on an unstructured finite-volume discretization of the domain was adopted to integrate the governing equations

[24]. The mesh contains 178607 cells and it is refined in the inflection region. The resolution was chosen by a grid convergence analysis performed for a previous study [38]. A plot of the dimensionless wall distance $y+$ is reported in Figure 4. A second order accurate spatial discretisation is adopted and the reconstruction required by convective fluxes is limited using the Barth-Jespersen technique [41], whereas the gradient required by diffusive fluxes and source terms is computed using the weighted least square method. Convective fluxes are evaluated using a hybrid solver [42] that combines Flux Difference Splitting [43, 44] and the local Lax-Friedrichs (or Rusanov) flux [45]. The computational domain is discretized using the Frontal-Delaunay for quads algorithm by the Gmsh tool [46]. The unstructured grid is managed in the parallel MPI environment via the DMPlex class [47] provided by the PETSc library [48].

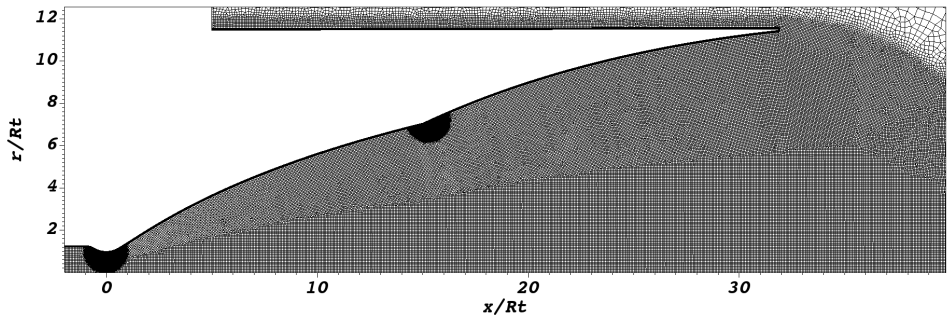

Figure 3: Detail on the mesh in the region inside the nozzle.

The flow field is investigated first without introducing the secondary injection. The Mach number contour lines at NPR=115 and NPR=185 are reported in Figure 5 which shows the low-altitude and the high-altitude working modes. The wall pressure p_w distribution normalised with respect to the chamber pressure p_c is reported in Figure 6: the plot shows that the RANS simulations predict the natural transition in the range $170 < NPR < 175$.

However, it is possible to observe a significant displacement of the separation line within the inflection region [10] when the NPR is increased from NPR=115 to NPR=170. In particular, the magnitude of the wall pressure gradient at the separation location can assume relatively small values when

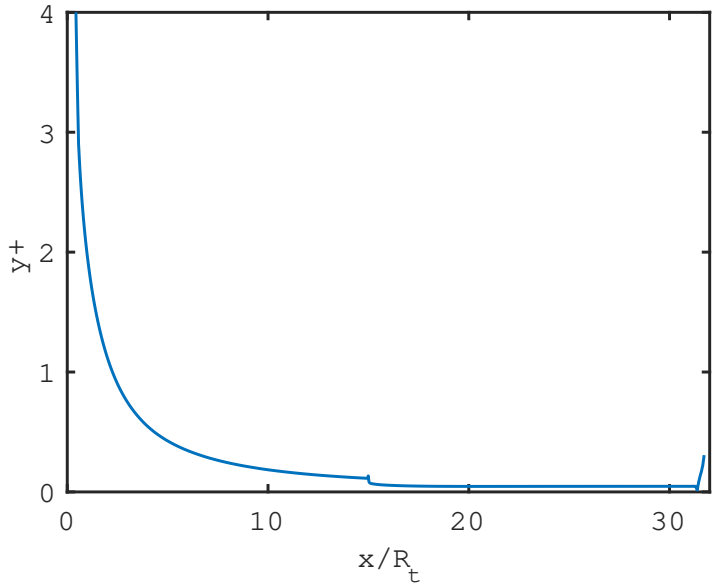

Figure 4: Dimensionless wall distance ($y+$) in full flow working condition (NPR=200 without control).

the NPRs increases from the sea-level condition to the transitional NPR. According to [36], the magnitude of the side loads increases when the magnitude of the wall pressure gradient upstream of the separation point decreases: this means that significant side loads could be obtained if natural transition occurs [17]. In particular, the magnitude of the nondimensional side loads Φ can be estimated according to [36] as:

$$\Phi = \frac{F_{sl}}{2k_g k_{sl} R_t^2 p_a} = \frac{r_s}{R_T}\frac{p_s}{p_c}\left(1-\frac{p_s}{p_a}\right)\frac{1}{\frac{dp_s/p_c}{d(l/R_t)}}\frac{1}{1-\frac{1+\frac{\gamma-1}{2}M_s^2}{(1.88M_s-1)M_i}\frac{1.2}{\gamma}} \tag{4}$$

where F_{sl}, r_s, p_s, $\frac{dp_s/p_c}{d(l/R_t)}$ and M_s represent side loads magnitude, radius, wall pressure, normalized wall pressure gradient magnitude and wall isentropic Mach number at the separation point, respectively. The values of the constants k_g and k_{sl} are provided by [36] but a large uncertainty characterizes these values. However, the values of these constants are not considered here since the goal of the present work is to compare the nondimensional side loads in the uncontrolled and controlled transition: the values of the constants disappear if the ratio of the side loads in the two configurations is

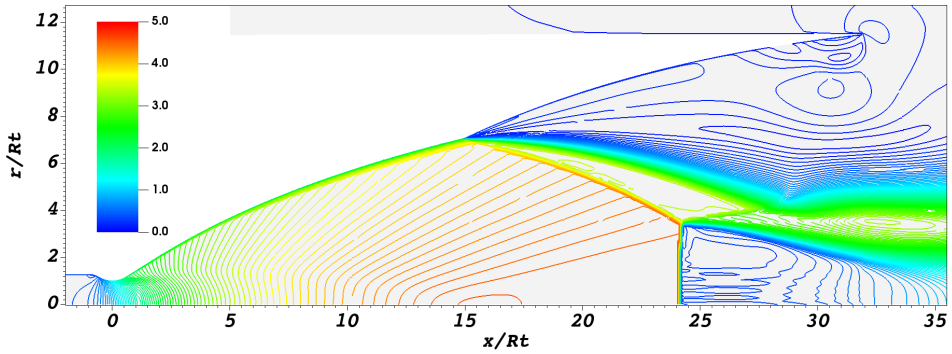

(a)

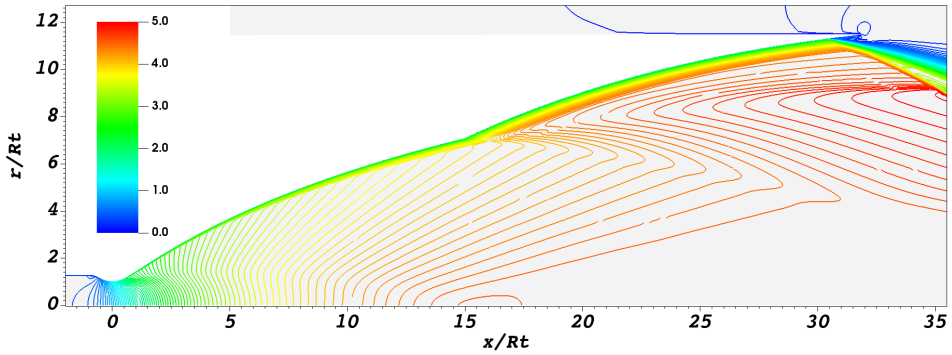

(b)

Figure 5: Mach number contour lines at NPR=115 (a) and NPR=185 (b) without control.

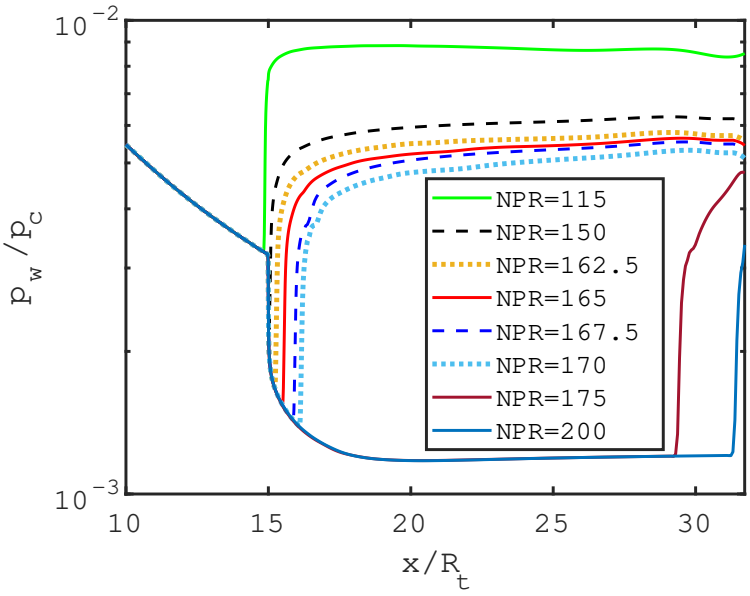

Figure 6: Wall pressure distribution in the optimized dual-bell nozzle for $115 < NPR < 175$ without control.

considered.

A second set of simulations is performed by activating the secondary injection to delay the transition. The secondary flow is radially injected at $x/R_t = 16$ through an annular slot (width equal to $0.073R_t$). The total temperature and total pressure of the injection are assumed to be equal to 300 K and 1.96 bar, respectively. The flow through the injection slot is assumed to be supersonic ($M_i = 2$). A discussion on the use of sonic or supersonic injection is reported in [38]. The effect induced by the secondary injection is evident in Figure 7 which shows the Mach number contour lines at NPR=200 for the uncontrolled and controlled configurations: the uncontrolled flow is reattached while the flow with the secondary injection is still separated. The plot shows that the secondary jet acts as an obstacle for the supersonic flow, inducing a fluidic ramp and keeping the separation fixed at the inflection point. A details of the Mach number contour lines in the region around the injection slot is reported in Figure 8.

More details can be deduced from the wall pressure distribution which is reported in Figure 9 for several values of NPR: the plot shows that the

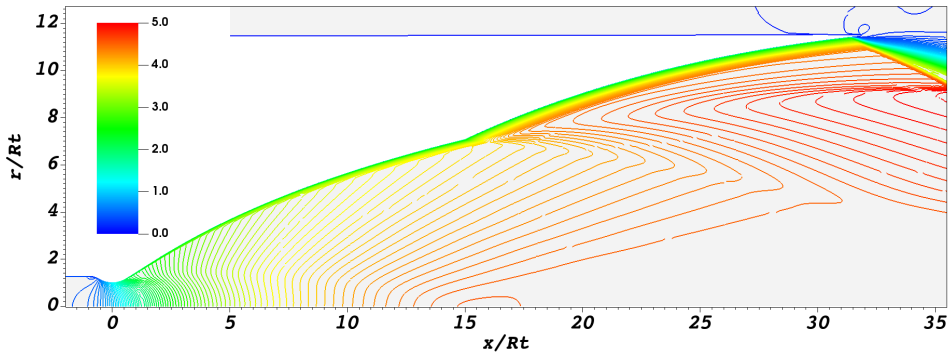

(a)

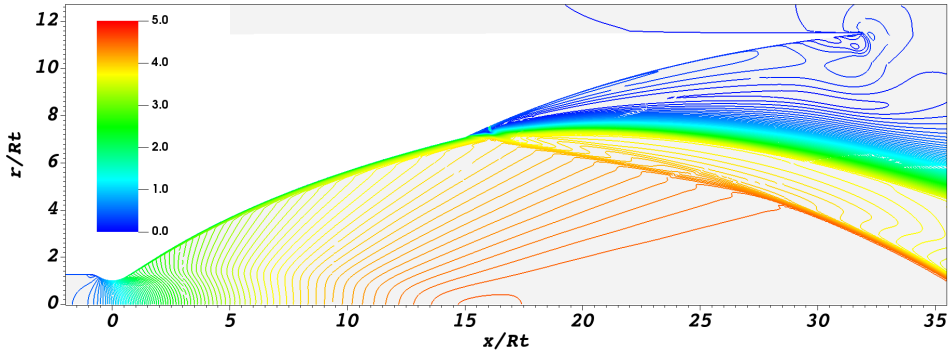

(b)

Figure 7: Mach number contour lines at NPR=200 without control (a) and with control (b).

separation line remains confined close to the inflection point for $NPR < 205$. This represents a significant extension of the transitional NPR with respect to the result obtained for the uncontrolled flow ($NPR < 175$). The effects of the secondary injection on the location of the separation line for several values of NPR is reported in Figure 10. Finally, the magnitude of the wall pressure gradient upstream of the separation line is systematically larger in the controlled flow with respect to the values observed for the natural transition. This means that in the controlled flow the magnitude of the side loads is expected to be reduced with respect to the uncontrolled configuration, according to Eq. 4. This is confirmed by the plot reported in Figure 11.

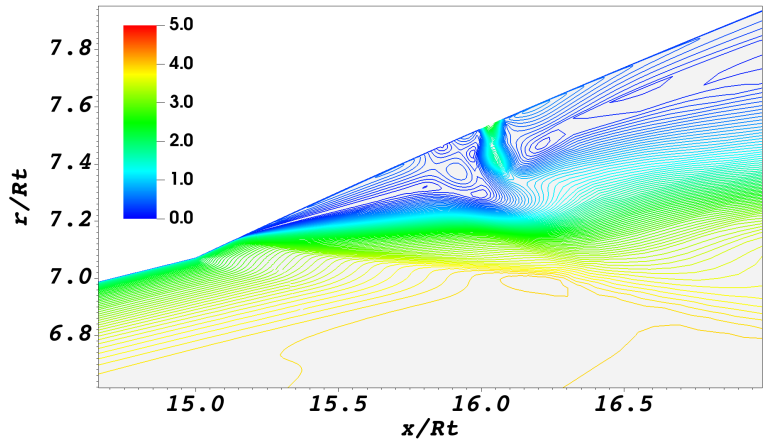

Figure 8: Mach number contour lines for the region near the injection slot at NPR=200.

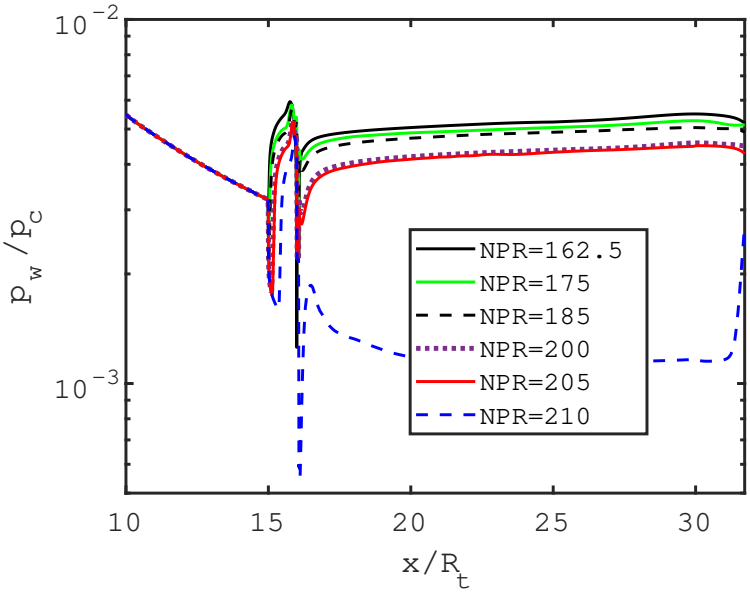

Figure 9: Wall pressure distribution in the optimized dual-bell nozzle for $175 < NPR < 220$ with secondary injection.

4. Corrections to the optimal solution

The CFD study enabled a more complete understanding of the control system requirements. In particular, the side loads estimation reported in

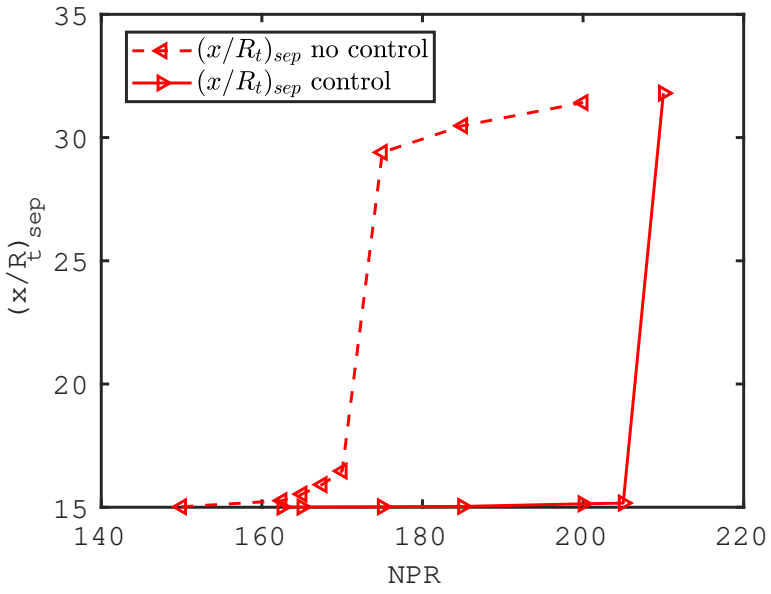

Figure 10: Separation location for uncontrolled and controlled flow.

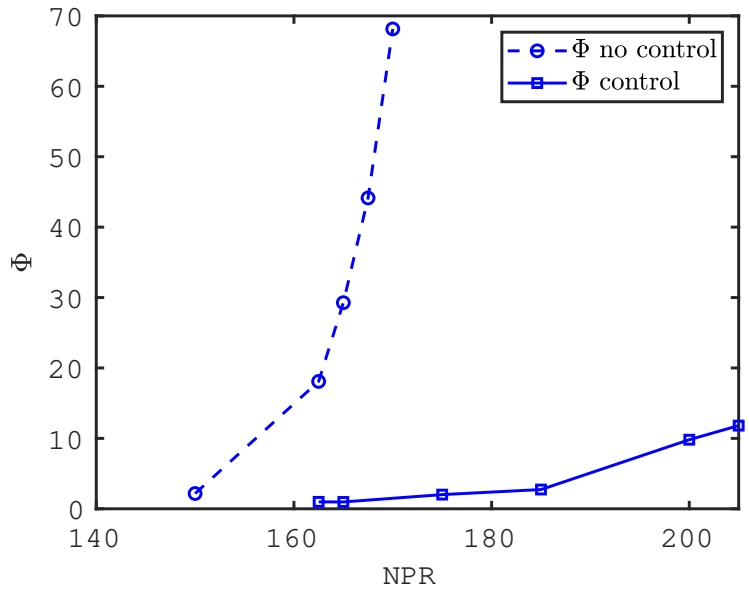

Figure 11: Nondimensional side loads for uncontrolled and controlled flow.

Figure 11 suggests the following choice: $NPR_{ON} = 160$ and $NPR_{OFF} = 200$. In this manner, the control system is activated before significant side loads are observed, and it is deactivated at a NPR significantly higher than the natural transitional NPR, resulting in a rapid transition to full flow working conditions.

The new NPR_{ON}, NPR_{OFF} and $\dot{m}_i = 0.0315\dot{m}$ are then used to run an updated trajectory optimisation analysis. A first optimal configuration is obtained by setting $m_{CS} = 500$ kg. Even if NPR_{OFF} was decreased from the optimal value (775) to a significantly lower but feasible value (200) the payload gain remains high ($\Delta m_{PL} = 1457$ kg). In this new configuration, the fluidic control system remains active for approximately 10 seconds when the launcher increases its altitude from 2 km to 4 km. The mass of the fluid injected in this time interval is relatively small (70 kg), especially if compared to the mass injected in the optimal configuration obtained by the preliminary study (230 kg). For this reason, a further trajectory optimisation was performed by reducing the mass budget allocated for the fluidic control system to m_{CS}=400 kg. This has a positive effect on the payload, which is increased further ($\Delta m_{PL} = 1497$ kg). In particular, the payload sensitivity with respect to the additional engine mass $\frac{\partial \Delta m_{PL}}{\partial m_{CS}} \approx 0.4$ is in line with the value (0.35) obtained by Stark et al.[30] through an analytical approach. Finally, in Figure 12 a plot of the altitude h as a function of time is reported and the key points of the mission are highlighted.

5. Conclusions

The benefits related to the use of the dual-bell nozzle in the core engine of a launcher inspired to the Ariane 5 are investigated by means of a parametric study in which both the nozzle geometry and the ascent trajectory were optimised. There are two main results in the present work. First of all, the study showed that significant payload gains can be obtained (approximately 1.5 ton in GTO for an Ariane-5 like launcher). The second result is related to the effectiveness of a secondary injection in controlling the separation position during the ascent: this is important because side loads can be a critical issue in the real application of a dual-bell. In particular, the simulations highlighted once more that, in the uncontrolled flow, the separation line moves in the inflection region where it is known that significant side loads can be generated. The use of a secondary injection performed downstream of the inflection point consent to significantly limit the displacement of the sepa-

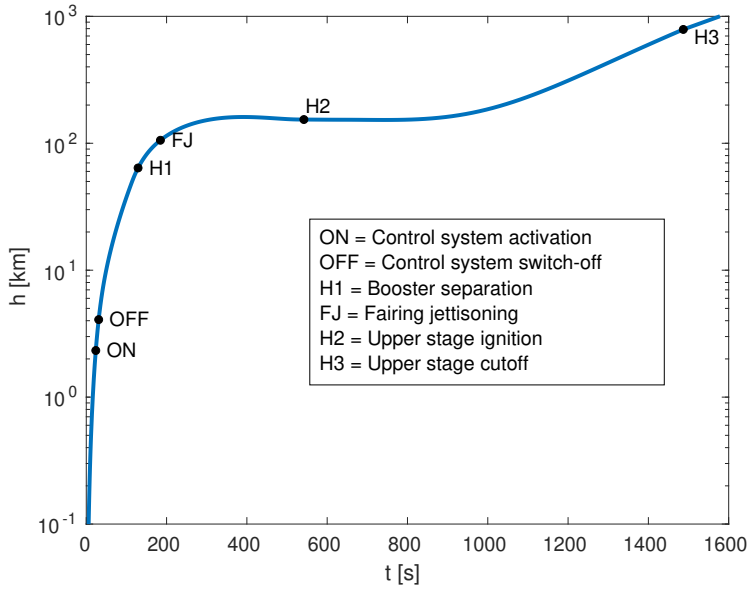

Figure 12: Optimal trajectory with controlled transition.

ration line, which remains in regions characterised by a large wall pressure gradient magnitude until the injection is deactivated. This feature could be very useful to synchronise the transition in a full-liquid configuration with multiple dual-bell nozzles. Furthermore, external pressure fluctuations can be observed during the ascent phase of a launcher and they can induce oscillations between the two working modes of the dual-bell nozzle [19]: the secondary injection could be useful also in this case to prevent the problem. The CFD simulations and the reduced activation time suggested that the control could be realised by the injection of a cold gas stored inside a dedicated tank. Alternative sources for the injected fluid will be investigated in the future, as well as, the effectiveness of fluidic control in the presence of reacting flows.

References

[1] G. Hagemann, H. Immich, T. Van Nguyen, G. E. Dumnov, Advanced rocket nozzles, Journal of Propulsion and Power 14 (5) (1998) 620–634. doi:10.2514/2.5354.

[2] G. Luke, D. Adams, Use of nozzle trip rings to reduce nozzle separation side force during staging, in: 28th Joint Propulsion Conference and Exhibit, 1992, p. 3617.

[3] N. Goncharov, V. Orlov, V. Rachuk, A. Shostak, R. Starke, Reusable launch vehicle propulsion based on the RD-0120 engine, in: 31st Joint Propulsion Conference and Exhibit, 1995, p. 3003. doi:10.2514/6.1995-3003.

[4] V. V. Semenov, A. A. Sergienko, Rocket engine laval nozzle with gas injection device (October 2008).
URL https://patents.google.com/patent/WO2008129372A3

[5] R. A. Wasko, Performance of annular plug and expansion-deflection nozzles including external flow effects at transonic mach numbers, NASA-TN-D-4462 (April 1968).

[6] M. Horn, S. Fisher, Dual-bell altitude compensating nozzles, Tech. rep., Rockwell International Corp., Canoga Park, CA, United States (1993).

[7] H. Immich, M. Caporicci, FESTIP technology developments in liquid rocket propulsion for reusable launch vehicles, in: 32nd Joint Propulsion Conference and Exhibit, 1997, p. 3113. doi:10.2514/6.1996-3113.

[8] M. Frey, G. Hagemann, Critical assessment of dual-bell nozzles, Journal of propulsion and power 15 (1) (1999) 137–143. doi:10.2514/2.5402.

[9] F. Nasuti, M. Onofri, Theoretical analysis and engineering modeling of flowfields in clustered module plug nozzles, Journal of Propulsion and Power 15 (4) (1999) 544–551. doi:10.2514/2.5477.

[10] F. Nasuti, M. Onofri, E. Martelli, Role of wall shape on the transition in axisymmetric dual-bell nozzles, Journal of propulsion and power 21 (2) (2005) 243–250. doi:10.2514/1.6524.

[11] E. Martelli, F. Nasuti, M. Onofri, Numerical parametric analysis of dual-bell nozzle flows, AIAA journal 45 (3) (2007) 640–650. doi:10.2514/1.26690.

[12] R. Parsley, K. van Stelle, Altitude compensating nozzle evaluation, in: 28th Joint Propulsion Conference and Exhibit, 1992, p. 3456. doi:10.2514/6.1992-3456.

[13] L. Boccaletto, J.-P. Dussauge, High-performance rocket nozzle concept, Journal of Propulsion and Power 26 (5) (2010) 969–979. doi:10.2514/1.48904.

[14] L. Casalino, D. Pastrone, F. Simeoni, Effects of limitation of nozzle flow separation on launcher performance, Journal of Propulsion and Power 29 (4) (2013) 849–854. doi:10.2514/1.B34669.

[15] A. Ferrero, D. Pastrone, Plasma actuator–assisted rocket nozzle for improved launcher performance, AIAA Journal 57 (4) (2019) 1348–1354. doi:10.2514/1.J057956.

[16] I. Ivanov, I. Kryukov, Numerical study of ways to prevent side loads in an over–expanded rocket nozzles during the launch stage, Acta Astronautica 163 (2019) 196–201. doi:10.1016/J.ACTAASTRO.2019.02.032.

[17] C. Genin, R. H. Stark, Side loads in subscale dual bell nozzles, Journal of Propulsion and Power 27 (4) (2011) 828–837. doi:10.2514/1.B34170.

[18] M. Cimini, E. Martelli, M. Bernardini, Numerical analysis of side-loads reduction in a sub-scale dual-bell rocket nozzle, Flow, Turbulence and Combustion (2021) 1–24doi:10.1007/s10494-021-00243-4.

[19] S. B. Verma, R. Stark, O. Haidn, Effect of ambient pressure fluctuations on dual-bell transition behavior, Journal of Propulsion and Power 30 (5) (2014) 1192–1198. doi:10.2514/1.B35067.

[20] S. Verma, R. Stark, O. Haidn, Reynolds number influence on dual-bell transition phenomena, Journal of Propulsion and Power 29 (3) (2013) 602–609. doi:10.2514/1.B34734.

[21] T. Tomita, M. Takahashi, M. Sasaki, Control of transition between two working modes of a dual-bell nozzle by gas injection, in: 45th AIAA/ASME/SAE/ASEE Joint Propulsion Conference & Exhibit, 2009, p. 4952. doi:10.2514/6.2009-4952.

[22] V. Zmijanovic, L. Leger, M. Sellam, A. Chpoun, Assessment of transition regimes in a dual-bell nozzle and possibility of active fluidic control, Aerospace Science and Technology 82 (2018) 1–8. doi:10.1016/j.ast.2018.02.003.

[23] L. Léger, V. Zmijanovic, M. Sellam, A. Chpoun, Controlled flow regime transition in a dual bell nozzle by secondary radial injection, Experiments in Fluids 61 (12) (2020) 1–15. doi:10.1007/s00348-020-03086-3.

[24] A. Ferrero, E. Martelli, F. Nasuti, D. Pastrone, Fluidic control of transition in a dual-bell nozzle, in: AIAA Propulsion and Energy 2020 Forum, 2020, p. 3788. doi:10.2514/6.2020-3788.

[25] L. Léger, V. Zmijanovic, M. Sellam, A. Chpoun, Experimental investigation of forced flow regime transition in a dual bell nozzle by secondary fluidic injection, International Journal of Heat and Fluid Flow 89 (2021) 108818. doi:10.1016/j.ijheatfluidflow.2021.108818.

[26] E. Martelli, F. Nasuti, M. Onofri, Film cooling effect on dual-bell nozzle flow transition, in: 45th AIAA/ASME/SAE/ASEE Joint Propulsion Conference & Exhibit, 2009, p. 4953. doi:10.2514/6.2009-4953.

[27] D. Proschanka, K. Yonezawa, H. Koga, Y. Tsujimoto, T. Kimura, K. Yokota, Control of operation mode transition in dual-bell nozzles with film cooling, Journal of Propulsion and Power 28 (3) (2012) 517–529. doi:10.2514/1.B34202.

[28] R. Stark, C. Génin, C. Mader, D. Maier, D. Schneider, M. Wohlhüter, Design of a film cooled dual-bell nozzle, Acta Astronautica 158 (2019) 342–350. doi:10.1016/j.actaastro.2018.05.056.

[29] D. Schneider, R. Stark, C. Génin, M. Oschwald, K. Kostyrkin, Active control of dual-bell nozzle operation mode transition by film cooling and mixture ratio variation, Journal of Propulsion and Power 36 (1) (2020) 47–58. doi:10.2514/1.B37299.

[30] R. Stark, C. Génin, D. Schneider, C. Fromm, Ariane 5 performance optimization using dual-bell nozzle extension, Journal of Spacecraft and Rockets 53 (4) (2016) 743–750. doi:10.2514/1.A33363.

[31] G. Colasurdo, D. Pastrone, Indirect optimization method for impulsive transfers, in: Astrodynamics Conference, 1994, p. 3762. doi:10.2514/6.1994-3762.

[32] Ariane 5 User's Manual, Arianespace, Evry-Courcouronnes, France, 2008.

[33] S. Isakowitz, J. Hopkins, J. Hopkins Jr, International Reference Guide to Space Launch Systems, American Institute of Aeronautics and Astronautics, Inc., 1994.

[34] A. E. Bryson, Y.-C. Ho, Applied optimal control, Hemisphere Publishing Co., 1975.

[35] L. Casalino, G. Colasurdo, D. Pastrone, Optimal low-thrust escape trajectories using gravity assist, Journal of Guidance, Control, and Dynamics 22 (5) (1999) 637–642. doi:10.2514/2.4451.

[36] R. H. Schmucker, Flow process in overexpanded chemical rocket nozzles. part 1: Flow separation, NASA TM-77396 (January 1984).

[37] P. E. Gill, W. Murray, M. H. Wright, Practical optimization, SIAM, 2019. doi:10.1137/1.9781611975604.

[38] A. Ferrero, A. Conte, E. Martelli, F. Nasuti, D. Pastrone, Dual-bell nozzle for space launchers with fluidic control of transition, in: AIAA Propulsion and Energy 2021 Forum, 2021, p. 3586. doi:10.2514/6.2021-3586.

[39] S. R. Allmaras, F. T. Johnson, Modifications and clarifications for the implementation of the Spalart-Allmaras turbulence model, in: Seventh international conference on computational fluid dynamics (ICCFD7), 2012, pp. 1–11.

[40] R. Paciorri, F. Sabetta, Compressibility correction for the Spalart-Allmaras model in free-shear flows, Journal of Spacecraft and Rockets 40 (3) (2003) 326–331. doi:10.2514/2.3967.

[41] T. Barth, D. Jespersen, The design and application of upwind schemes on unstructured meshes, in: 27th Aerospace sciences meeting, 1989, p. 366. doi:10.2514/6.1989-366.

[42] A. Ferrero, D. D'Ambrosio, A hybrid numerical flux for supersonic flows with application to rocket nozzles, Advances in Aircraft and Spacecraft Science 7 (5) (2020) 387–404. doi:10.1063/5.0026763.

[43] S. Osher, F. Solomon, Upwind difference schemes for hyperbolic systems of conservation laws, Mathematics of computation 38 (158) (1982) 339–374. doi:10.2307/2007275.

[44] M. Pandolfi, A contribution to the numerical prediction of unsteady flows, AIAA journal 22 (5) (1984) 602–610. doi:10.2514/3.48491.

[45] V. V. Rusanov, The calculation of the interaction of non-stationary shock waves and obstacles, USSR Computational Mathematics and Mathematical Physics 1 (2) (1962) 304–320. doi:10.1016/0041-5553(62)90062-9.

[46] C. Geuzaine, J.-F. Remacle, Gmsh: A 3-D finite element mesh generator with built-in pre-and post-processing facilities, International journal for numerical methods in engineering 79 (11) (2009) 1309–1331. doi:10.1002/nme.2579.

[47] M. Lange, M. G. Knepley, G. J. Gorman, Flexible, scalable mesh and data management using petsc dmplex, in: Proceedings of the 3rd International Conference on Exascale Applications and Software, University of Edinburgh, 2015, pp. 71–76.

[48] S. Balay, S. Abhyankar, M. Adams, J. Brown, P. Brune, K. Buschelman, L. Dalcin, A. Dener, V. Eijkhout, W. Gropp, et al., PETSc users manual (2019).